

Numerical Computation of Hydrodynamic Loads on Walls of a Rigid Rectangular Tank Due to Large Amplitude Liquid Sloshing

Hakan AKYILDIZ, M. Serdar ÇELEBİ

*İstanbul Technical University, Faculty of Naval Architecture
and Ocean Engineering, 80626, Maslak, İstanbul-TURKEY
e-mail: akyildiz@itu.edu.tr*

Received 26.11.2001

Abstract

Liquid sloshing in a moving partially filled rectangular tank have been investigated. Sloshing in a rectangular tank is a non-linear phenomenon. When the amplitude of tank oscillation is large, two types of non-linearities are present. One occurs at the free surface due to the large fluid motion. The other occurs at the fluid-tank interface. A numerical algorithm based on the volume of fluid (VOF) technique is used to study the non-linear behavior and damping characteristics of liquid sloshing in partially filled rectangular tanks subjected to large amplitude excitation. The excitation is assumed to be harmonic to simulate tank motion. The fluid is assumed to be homogeneous, isotropic, viscous, and Newtonian and exhibits only limited compressibility. Tank and fluid motions are assumed to be two-dimensional. A moving coordinate system is used to include the non-linearity and avoid the complex boundary conditions of moving walls. The numerical model solves the complete Navier-Stokes equations in primitive variables by using of the finite difference approximations. The VOF technique is used to track the free surface and, at each time step, a donor-acceptor method is used to transport the volume of fluid function and hence the locations of the free surface. The numerical method also allows the interaction of the fluid with the tank top. In order to assess the accuracy of the method used, computations are compared with the experimental results. Comparisons show good agreement for both impact and non- impact type slosh loads in the cases investigated.

Key words: Sloshing, Hydrodynamic loads, Free surface flow, Volume of fluid technique method

Introduction

Liquid sloshing in a moving container can be associated with various engineering problems, such as liquid oscillations in large storage tanks caused by earthquakes, motions of liquid fuel in aircraft and spacecraft, liquid motions in containers and water flow on the decks of ships. Large liquid movements create highly localized impact pressure on tank walls that may in turn cause structural damage and may even create sufficient moment to affect the stability of the vehicle carries the container. As is well known, this is a difficult mathematical problem to be solved numerically as well as analytically. There are two major problems that arise in a computa-

tional approach to sloshing: first, the nonlinear moving boundary conditions at the fluid tank interface, and second, the nonlinear motion of the free surface is not known *a priori*.

There has been a considerable amount of work on liquid sloshing. Most of these studies are reported in a recent paper by Ibrahim, *et al.* (2001). A liquid's motion inside container has an infinite number of natural frequencies, but it is the lowest few modes that are most likely to be excited by the motion of a vehicle. Most studies have therefore concentrated on investigating forced harmonic oscillations near the lowest natural frequency, predicted by fluid field linear equations. However, nonlinear effects result in the frequency of maximum response being slightly

different from the linear natural frequency and they depend on amplitude. Nonlinear effects include amplitude jump, parametric resonance, chaotic liquid surface motion, and nonlinear sloshing mode interaction (internal resonance among the liquid sloshing modes).

Analytical solutions are limited to regular geometric tank shapes, such as cylindrical and rectangular. The nature of sloshing dynamics in cylindrical tanks is better understood than for prismatic tanks. However, analytical techniques for predicting large-amplitude sloshing are still not fully developed. Such loads are extremely important in the design stage of the supporting structure and internal components of vehicle tanks.

Lui and Lou (1990) studied the dynamic coupling of a liquid-tank system under transient excitation analytically for a two-dimensional rectangular rigid tank with no baffles. They showed that the discrepancy of responses in the two systems can obviously be observed when the ratio of the natural frequency of the fluid and the natural frequency of the tank are close to unity. Sloshing phenomena in moving rectangular tanks can usually be described by considering only two-dimensional fluid flow. Sloshing in spherical or cylindrical tanks, however, usually must involve three-dimensional flow effects. Tanks with a two-dimensional flow are divided into two classes: low and high liquid fill depths. The low fill depth case is represented by $D/2a < 0.2$, where D is the still liquid depth and $2a$ is the tank width in the direction of the motion. The low fill depth case is characterized by the formation of hydraulic jumps and traveling waves for excitation periods around resonance. At higher fill depths, large standing waves are usually formed in the resonance frequency range. When hydraulic jumps or traveling waves are present, extremely high impact pressures can occur on the tank walls (Akyıldız and Çelebi, 2001a).

In their recent paper, Faltinsen and Timokha (2001), analyzed the two-dimensional nonlinear sloshing of an incompressible fluid with irrotational flow in a rectangular tank by a modal theory. The theory they used is in good agreement with experimental results but the model assumes infinite tank roof height.

Çelebi and Akyıldız (2001) investigated the nonlinear modeling of liquid sloshing in a tank forced to move harmonically along a vertical curve with a rolling motion in order to simulate actual tank excitation on the road. They concluded that, in an

increased fill depth, the rolling amplitude and frequency of the tank with/without baffle configuration directly affect the degree of non linearity of the sloshing phenomena. As a result of this, phase shifting in forces and moments occurred.

Akyıldız and Çelebi (2001b) investigated the numerical computation of pressure in a rigid rectangular tank due to large amplitude liquid sloshing. They modeled the same problem with different tank configurations including baffled and unbaffled tanks. The present work extends this study for computing the wave run-ups, forces and moments on a tank's walls. Additionally, the same computations are performed for both first- and second-order finite difference approximations to observe the numerical improvement on the results of the numerical model used.

Finite Difference Form of the Equation of the Sloshing Motion

The fluid is assumed to be homogeneous, isotropic, viscous and Newtonian and exhibits only limited compressibility. Tank and fluid motions are assumed to be two-dimensional, which implies that there is no variation of fluid properties or flow parameters in one of the coordinate directions. The domain considered here is a rigid rectangular container with and without baffle configuration partially filled with liquid.

The governing equations, namely the Navier-Stokes and continuity equations, are solved simultaneously with the corresponding boundary conditions and free surface kinematic and dynamic boundary conditions given in our previous paper (Akyıldız and Çelebi, 2001b).

In order to include the nonlinearity and avoid the complex boundary conditions of moving walls, the moving coordinate system is used. The origin of the coordinate system is in the position of the center plane of the tank and in the undisturbed free surface. The moving coordinate is translating and rotating relative to an inertial system (see Figure 1). The equilibrium position of the tank relative to the axis of rotation is defined by ϕ . For instance, the tank is rotating about a fixed point on the y-axis at $\phi = 90^\circ$. Thus, the moving coordinate system can be used to represent the general roll (displayed by θ) or pitch of the tank.

A non-uniform finite difference mesh is used, consisting of an Eulerian grid of fixed rectangular cells. The mesh region containing fluid is composed of cells

labeled with the index i in the x -direction, the cells labeled with the index j in the y -direction. A single layer of fictitious cells (or boundary cells) surrounds the fluid region. The fictitious cells are used to set the boundary conditions so that the same difference equation can be used in the interior of the mesh (see Figure 2).

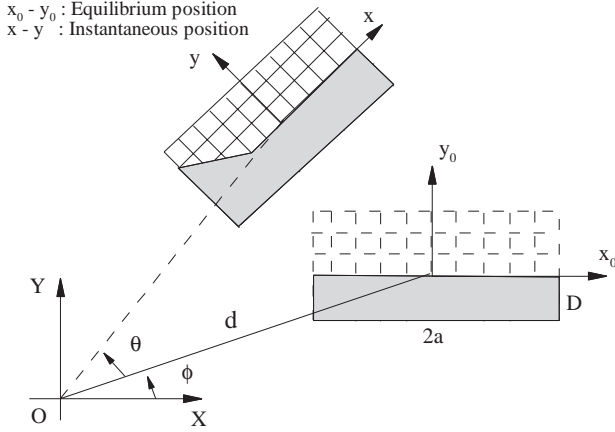


Figure 1. The moving coordinate system

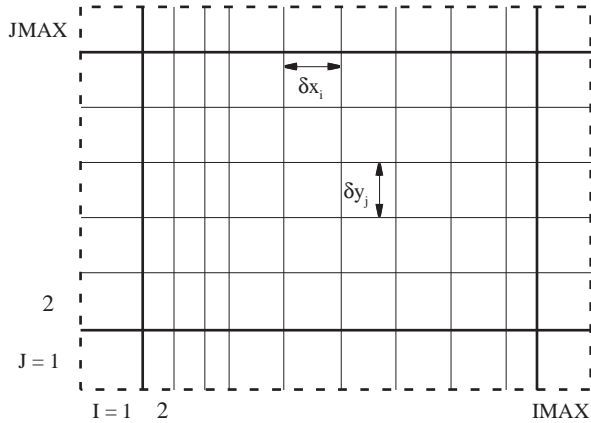


Figure 2. General mesh arrangement. Fictitious boundaries are dashed.

Fluid velocities are located at the middle of the sides of the cell: U -velocity at the middle of the vertical side and V -velocity at the middle of the horizontal side. The pressure (P) and the volume of fluid function (F) are also located at the cell center (see Figure 3).

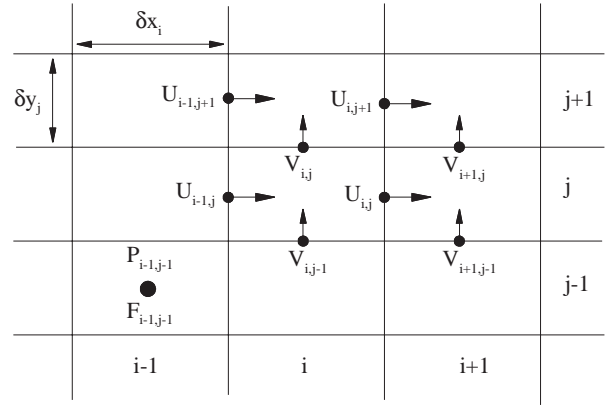


Figure 3. Arrangement of finite difference variables.

By making each cell a local control volume, the continuity equation becomes cell centered. Thus, it becomes convenient to center the x -momentum difference equation at the right cell face and the y -momentum at the upper cell face. This is convenient because the pressure gradients along with the other momentum terms can be conveniently centered at the cell walls. In the difference approximations, subscripts are used for the cell locations and superscripts for the time level at which quantities are evaluated such that $t = n \delta t$, where δt is the average time increment. For instance, the difference approximation representing the continuity equation for a typical cell is

$$\frac{1}{\delta x_i} (U_{i,j}^{n+1} - U_{i-1,j}^{n+1}) + \frac{1}{\delta y_j} (V_{i,j}^{n+1} - V_{i,j-1}^{n+1}) + \frac{1}{c^2 \delta t} (P_{i,j}^{n+1} - P_{i,j}^n) = 0 \quad (1)$$

For the hydrodynamic forces and moments, it is integrated over the tank walls. A trapezoidal approximation is used, i.e. the force on a cell face is just the pressure in the cell center times the length of the cell face. In partially filled cells a hydrostatic approximation is used. The force on a cell face is approximated as follows:

$$\text{FORCE}_j = \frac{\gamma}{2} \cdot (F_{i,j} \times \text{DELY}_j)^2 \quad (2)$$

where γ is the fluid specific weight, $F_{i,j}$ is the function representing the fractional volume of the fluid and DELY_j is the mesh spacing along the y -axis. The moments can also be used for the determination of overturning moments in car tanks or stability effects on cargo ships.

Procedure of computation

The solution algorithm works as a time cycle or ‘movie frame’. The results of the time cycle act as initial conditions for the next one. At each time step the following computations are performed:

(a) Explicit approximations of the velocity field from the momentum equations use old time level values for the advective, viscous, coriolis terms and time centered values for the other apparent body forces. Since the pressure is evaluated implicitly, the new velocities make two contributions. This can be easily explained using the x-momentum as an example:

$$U_{i,j}^{n+1} = U_{i,j}^* + \frac{\delta t}{\delta x_{i+1/2}} [P_{i,j}^{n+1} - P_{i+1,j}^{n+1}] \quad (3)$$

where $U_{i,j}^*$ includes the viscous, advective and body force contributions to the updated momentum field. The new pressure gradients can be broken into two parts

$$P_{i,j}^{n+1} = P_{i,j}^n + \delta P_{i,j} \quad (4)$$

Substituting this expression into Equation (3) gives

$$U_{i,j}^{n+1} = U_{i,j}^* + \frac{\delta t}{\delta x_{i+1/2}} [P_{i,j}^n - P_{i+1,j}^n] + \frac{\delta t}{\delta x_{i+1/2}} [\delta P_{i,j} - \delta P_{i+1,j}] \quad (5)$$

$$U_{i,j}^{n+1} = \tilde{U}_{i,j} + \frac{\delta t}{\delta x_{i+1/2}} [\delta P_{i,j} - \delta P_{i+1,j}] \quad (6)$$

In the above equation, the first term on the right-hand side is added from the subroutine that calculates velocities while the second term is calculated in step (b) below the procedure and is subsequently added to the velocity field.

(b) For each cell, the change in pressure, δP , is calculated and added to the old pressure. This pressure is found by driving the velocity divergence to zero in each cell. Therefore, the continuity equation is first satisfied, and then the new pressure field is calculated and the additional pressure contribution is added into the velocity field. Iteration is required since adjacent cells are coupled. After the completion of this step, the new pressure and velocity field is known. At each step, suitable boundary conditions must be imposed at all boundaries.

Free surface problem

The location of the free surface as a function of time is not known *a priori* in the sloshing problem. In the process of embedding a discontinuous free surface in a matrix of computational cells, it is necessary to devise a way to numerically describe the location and shape of the boundary. The method that defines fluid regions rather than interfaces offers the advantage of logical simplicity. That is, it follows regions rather than surfaces and thus all logical problems associated with the intersecting surfaces are avoided. Furthermore, this method shares the region defining property without excessive use of a computer. The method is also applicable to three-dimensional computations, in which its conservative use of stored information is advantageous. Therefore, this method was used to compute the sloshing problem. In the method of the volume of the fluid, a function representing the fractional volume of fluid, $F(x,y,t)$, is defined whose value is unity at any point occupied by fluid and zero elsewhere. The average value of F in a cell would then represent the fractional volume of the cell occupied by the fluid.

Advancement of the Volume of the Fluid Function The time dependence function F is governed by the Eulerian conservation equation in two dimensions:

$$\frac{\partial F}{\partial t} + \vec{U} \cdot \nabla F = 0 \quad (7a)$$

or,

$$\frac{\partial F}{\partial t} + \frac{\partial}{\partial x} (U \cdot F) + \frac{\partial}{\partial y} (V \cdot F) = 0 \quad (7b)$$

In the above equations, U is the horizontal velocity of the fluid and V is the vertical velocity of the fluid. These equations, in divergence form, are convenient for numerical approximation, because changes in F in a cell reduce to fluxes of F across the cell faces. Since F is a step function, fluxes must be computed carefully to avoid the smearing of the discontinuities. Here, a mixed stream differencing method (donor-acceptor method) is used. Generally, a pure acceptor method is unstable due to negative diffusion, but the donar-acceptor method uses some simple tests to determine more accurately the location of the fluid in a cell. All cells are updated as the rows are swept. The donor and acceptor cells are determined by the direction of the velocity between the cells (Figure 4).

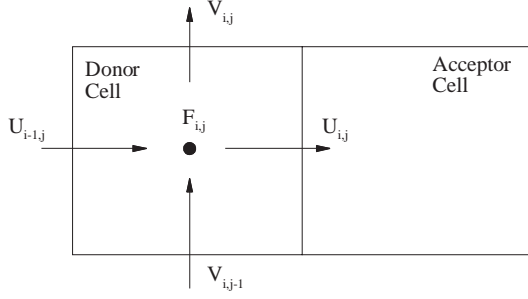


Figure 4. The donor and acceptor cells

There are three cases that demonstrate how the method transports the fluid as follows:

(a) The cell and its four surrounding cells are full of fluid and thus the flux is computed in four separate contributions. The total becomes

$$\frac{\partial F}{\partial t} = - \left[\frac{U_{i,j}^n \cdot F_{i+1,j}^n - U_{i-1,j}^n \cdot F_{i,j}^n}{\delta x_i} + \frac{V_{i,j}^n \cdot F_{i,j+1}^n - V_{i,j-1}^n \cdot F_{i,j}^n}{\delta y_j} \right] \quad (8)$$

Special care must be taken to satisfy the divergence of the velocity for an incompressible fluid, since the cells are full of fluid represented by $F = 1.0$.

(b) When the surface is advecting parallel or nearly parallel to itself and the acceptor cell is not empty, pure donor cell differencing is used. However, if the acceptor cell is empty, then the acceptor method is used. This means that a donor cell must fill before any fluid can enter a downstream empty cell. In this case, the x-direction flux becomes simple upstream differencing

$$\frac{\partial F}{\partial t} = - \frac{\partial}{\partial x}(UF) = - \left[\frac{U_{i,j}^n \cdot F_{i,j}^n - U_{i-1,j}^n \cdot F_{i-1,j}^n}{\delta x_i} \right] \quad (9)$$

The flux in the y-direction must also be computed.

(c) The vertical flux would be computed using the acceptor method because the surface is advecting normal to itself. The general acceptor method is used to advect in surface cells when: (i) The surface is advecting parallel to itself and the acceptor cell is empty; (ii) The surface is advecting normal to itself; and (iii) The cell downstream of the donor cell is empty.

The flux of F through a cell face is calculated for each cell. For the i,j 'th cell, the flux at the right interface is subtracted from the donor cell and added to the acceptor cell.

$$F_A = F_A + \frac{\partial F}{\partial x_A}, F_D = F_D - \frac{\partial F}{\partial x_D} \quad (10)$$

where

$$\partial F = \text{MIN} \{ (F_A \cdot |U_{i,j}| \cdot \partial t + CF), (F_D \cdot \partial x_D) \} \quad (11)$$

$$CF = \text{MAX} \{ [(1.0 - F_A) \cdot |U_{i,j}| \cdot \partial t - (1.0 - F_D) \cdot \partial x_D], 0.0 \} \quad (12)$$

where F_A and F_D values are the acceptor and the donor cells, respectively. Furthermore, the MIN feature prevents the fluxing of more fluid from the donor cell than it has to give, while the MAX feature accounts for an additional F flux if the amount of void $(1.0 - F)$ to be fluxed exceeds the amount available. A similar equation is used for the y-flux. When all the cell boundaries in the mesh have been updated, the resulting field of F corresponds to the time-advanced location of the interfaces.

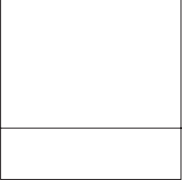
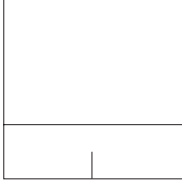
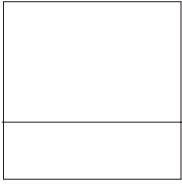
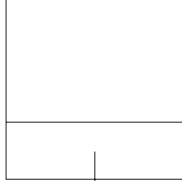
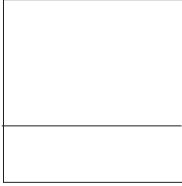
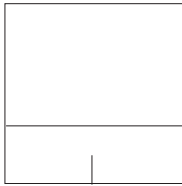
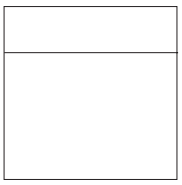
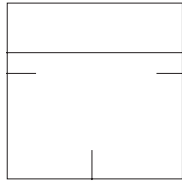
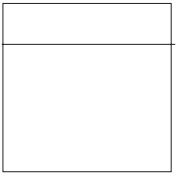
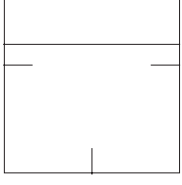
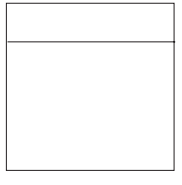
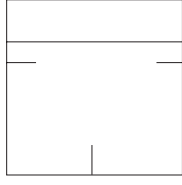
Numerical Implementations – Case Studies

Base of analysis

Twelve cases of computation were studied as shown in Table 1. It was assumed that the mesh dimensions would be small enough to resolve the main feature of liquid sloshing in each case. The step of time advance, Δt , in each cycle was also assumed to be so small that no significant flow change would occur during Δt . There was no case where a steady state solution was reached during the forcing periods used. Either instability set in or computer time became excessive, so the duration of computation was limited for each case. Therefore, computations were halted when the fluid particles extremely interacted and sprayed over the topside of the tank during extreme sloshing

When the frequency of the tank motion approaches one of the natural frequencies of the tank fluid, large sloshing amplitudes result. For a given tank geometry, the natural frequencies of the fluid depend on the fill depth and can be calculated from linear theories (Su *et al.* 1982). For rectangular prismatic tanks, the natural frequencies are given by

Table 1. Cases of computations (mesh dimensions = 41 x 30, H = height of the tank)

<p>Case (a)</p>  <p>Tank Dim. = 18*18 m Fill Depth = 0.25*H</p> <p>$\omega_R = \omega_n = 1.0596$ rad/s</p> <p>$\theta_0 = 4^\circ$</p>	<p>Case (b)</p>  <p>Tank Dim. = 18*18 m Fill Depth = 0.25*H</p> <p>$\omega_R = \omega_n = 1.0596$ rad/s</p> <p>$\theta_0 = 4^\circ$</p>
<p>Case (c)</p>  <p>Tank Dim. = 18*18 m Fill Depth = 0.25*H</p> <p>$\omega_R = 0.95 \omega_n = 1.00662$</p> <p>$\theta_0 = 4^\circ$</p>	<p>Case (d)</p>  <p>Tank Dim. = 18*18 m Fill Depth = 0.25*H</p> <p>$\omega_R = 0.95 \omega_n$</p> <p>$\theta_0 = 4^\circ$</p>
<p>Case (e)</p>  <p>Tank Dim. = 18*18 m Fill Depth = 0.25*H</p> <p>$\omega_R = 0.85 \omega_n = 0.90066$</p> <p>$\theta_0 = 4^\circ$</p>	<p>Case (f)</p>  <p>Tank Dim. = 18*18 m Fill Depth = 0.25*H</p> <p>$\omega_R = 0.85 \omega_n$</p> <p>$\theta_0 = 4^\circ$</p>
<p>Case (g)</p>  <p>Tank Dim. = 18*18 m Fill Depth = 0.75*H</p> <p>$\omega_R = \omega_n = 1.2968$ rad/s</p> <p>$\theta_0 = 4^\circ$</p>	<p>Case (h)</p>  <p>Tank Dim. = 18*18 m Fill Depth = 0.75*H</p> <p>$\omega_R = \omega_n = 1.2968$ rad/s</p> <p>$\theta_0 = 4^\circ$</p>
<p>Case (i)</p>  <p>Tank Dim. = 18*18 m Fill Depth = 0.75*H</p> <p>$\omega_R = 0.95 \omega_n = 1.23196$</p> <p>$\theta_0 = 4^\circ$</p>	<p>Case (j)</p>  <p>Tank Dim. = 18*18 m Fill Depth = 0.75*H</p> <p>$\omega_R = 0.95 \omega_n$</p> <p>$\theta_0 = 4^\circ$</p>
<p>Case (k)</p>  <p>Tank Dim. = 18*18 m Fill Depth = 0.75*H</p> <p>$\omega_R = 0.85 \omega_n = 1.10228$</p> <p>$\theta_0 = 4^\circ$</p>	<p>Case (l)</p>  <p>Tank Dim. = 18*18 m Fill Depth = 0.75*H</p> <p>$\omega_R = 0.85 \omega_n$</p> <p>$\theta_0 = 4^\circ$</p>

$$\omega_n^2 = g \frac{n\pi}{2a} \tanh\left(\frac{n\pi D}{2a}\right) \quad (13)$$

where g is the gravitational acceleration, $2a$ is the tank width, D is the water depth and n is the mode number. As seen from the above equation, an infinite number of natural frequencies exist. However, only the fundamental frequency ($n = 1$) is significant for marine engineering applications (Su *et al.* 1982; Lou *et al.* 1980).

In all cases, the tank started to roll about the center of the tank bottom at time $t = 0^+$. Since the major concern is to find the peak pressures on the left side of the tank on the free surface, the analysis is based on the comparison of the positive maximum pressures above the calm free surface for the various cases computed.

Comparison of the hydrodynamic loads of unbaffled and baffled cases in shallow liquid sloshing

Cases (a), (c) and (e) in Table 1 are the simulation in an unbaffled tank with a roll amplitude of 4° and roll frequency ω_R equal to natural frequency ω_n , $0.95\omega_n$ and $0.85\omega_n$, respectively. In a similar roll amplitude and frequency, the cases (b), (d) and (f) are of a baffled tank. The natural frequency of these cases is $\omega_n = 1.0596$ rad/sec. A snapshot for numerical simulation of the sloshing is displayed in Figure 5. The comparisons for the above cases are performed based on first- and second-order finite-difference approximations.

Figures 6(a) and (e) show maximum wave elevations for different rolling frequencies normalized by $2a$ (tank length). In Figure 6(a), for the unbaffled tank, the maximum wave height and the phase shifting increase as the rolling frequency increases. In Figure 6(e), for the baffled tank, the maximum wave elevations are significantly reduced. For example, wave crests and troughs are 81% and 56% decreased respectively for the case of $\omega_R = \omega_n$. The effect of rolling frequency on run-ups and phase shifting is not clearly observed as in Figure 6(a).

The normalized pressures ($P/2\gamma a\theta_0$), here γ is the specific weight of the fluid and θ_0 is the rolling amplitude, in Figures 6(b) and (f) are compared. Results show that with the increasing rolling frequency phase shifting occurs and the maximum pressure is reduced around 80%. The normalized forces and moments ($F/0.5\rho g D^2\theta_0$, $M/0.5\rho g D^3\theta_0$) in Figures 6(c)

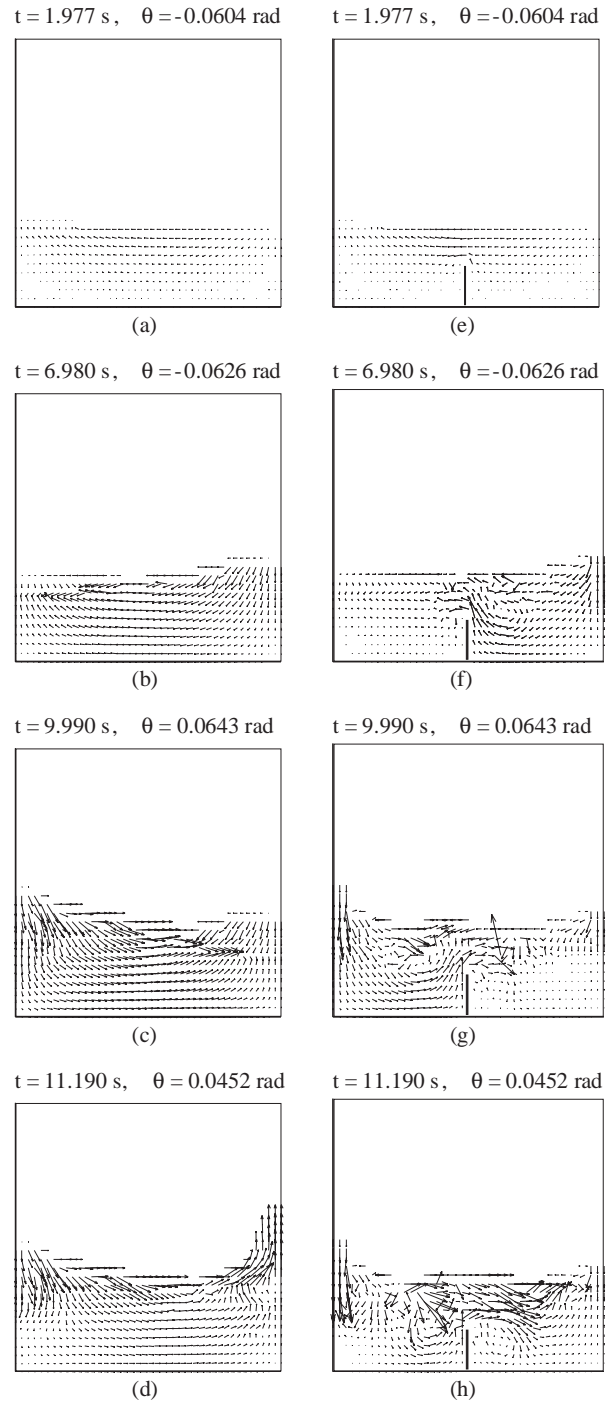


Figure 5. A snapshot for numerical simulation of the sloshing (unbaffled and baffled). ($\omega_R = \omega_n = 1.0596$ rad/s, $\theta_0 = 0.0698$ rad, $D = 0.25 \cdot H$)

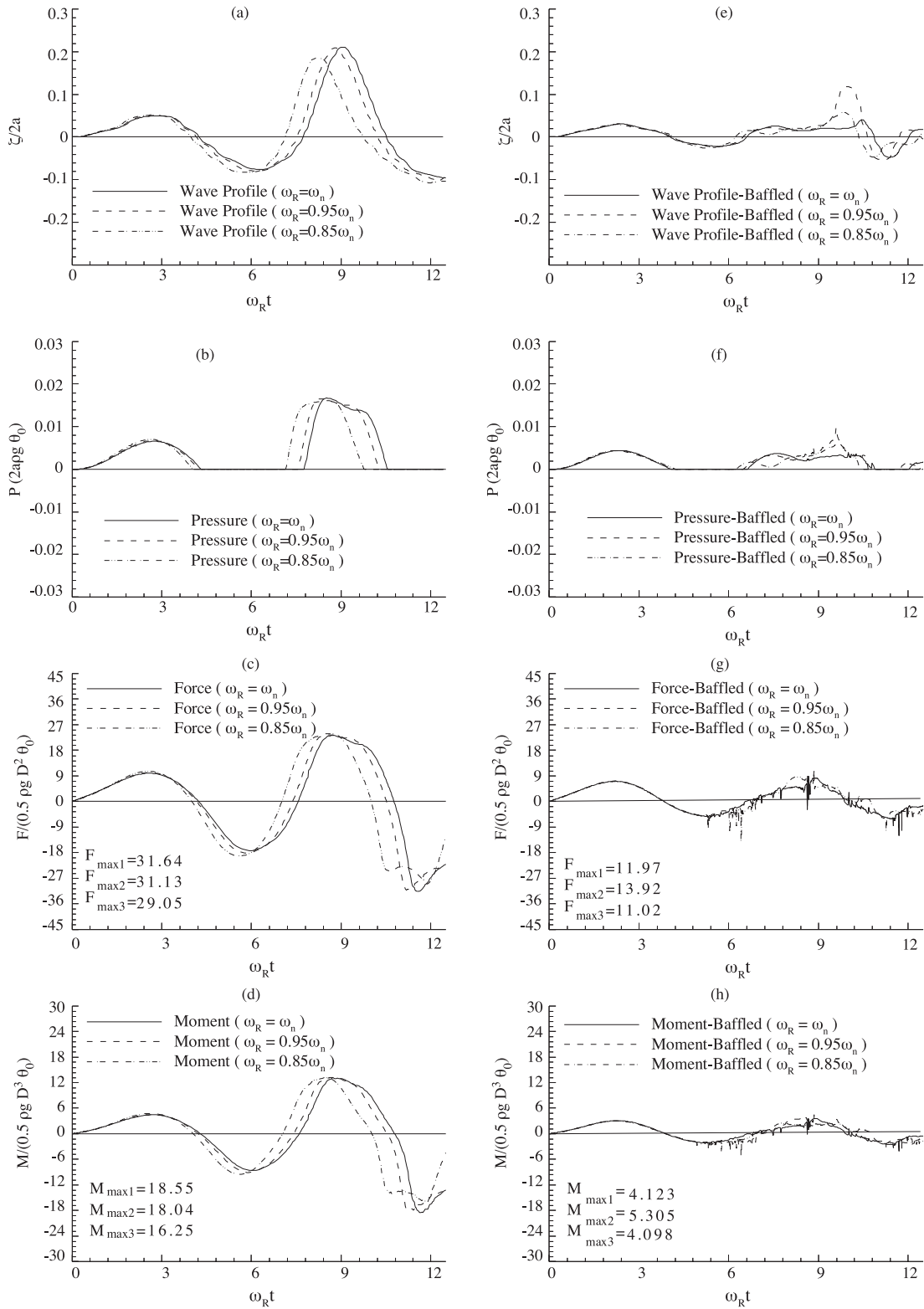


Figure 6. Comparison of the un baffled and baffled cases. First-order approximation. ($\omega_n = 1.0596$ rad/s, $\theta_0 = 4^\circ$, $D = 0.25 \cdot H$)

and 6(d) show that phase shifting is significant (for the third crossover, there is a 7% phase shift difference between $\omega_R = \omega_n$ and $\omega_R = 0.85\omega_n$) for the unbaffled case. The maximum pressure is increased as the rolling frequency increases. The effect of the baffle is observed to reduce the magnitudes of forces and moments and fluctuations around $\omega_R t > 5.0$ due to highly localized impacts resulting from eddies.

The second-order finite difference approximations in Figure 7 show that the magnitudes of the hydrodynamic loads and wave elevation in the baffled cases are significantly increased (for the case of $\omega_R = \omega_n$, maximum force and moment are 65% and 158% increased respectively) compared to the first-order finite difference approximation, while the unbaffled case slightly increased. One possible reason is that instantly changing velocity gradients near the baffle are approximated more accurately by the second-order formulation. Figure 8 shows these comparisons for the special case ($\omega_R = \omega_n$).

Comparison of the hydrodynamic loads of unbaffled and baffled cases in deep water sloshing

Cases (g), (i) and (k) in Table 1 represent the simulation in an unbaffled tank, with a roll amplitude of 4° and roll frequency ω_R equal to natural frequency ω_n , $0.95\omega_n$ and $0.85\omega_n$, respectively. Similarly, cases (h), (j) and (l) are of a baffled tank with the same rolling frequencies and amplitude. The natural frequency of these cases is $\omega_n = 1.2968$ rad/s. A snapshot for the simulation is shown in Figure 9. The comparisons are carried out based on first- and second-order finite-difference approximations.

Figures 10(a) and (e) show that maximum wave elevations for different rolling frequencies shift with the increasing $\omega_R t$. For deep water simulation, the wave interaction with the tank top is represented by the flat part of the curve.

Figures 10(b), (c), (d), (f), (g), and (h) show that the baffle effect in deep water simulation is less than those from the shallow water simulation. Results also show that the oscillations on the curves representing sloshing effects are much less compared with the shallow water. The same effects are also observed in the simulations using the second-order finite difference approximation in Figure 11. Two distinct differences are observed between first- and second-order approximations. First, the magnitudes of hydrodynamic loads in second-order simulations are slightly higher due to the increasing accuracy in derivatives. Second, the oscillations especially in baffled cases for

the second-order approximation are higher than the first-order. One possible reason is that the approximation of velocity and pressure gradients is better correlated with the second-order formula using the information from larger points.

For deep water sloshing, the comparisons between first- and second-order approximations are shown in Figure 12 for a resonant case.

Comparisons with Numerical and Experimental Results

The numerical results using both first- and second-order approximations under combined roll and vertical excitations are compared with the experimental results given in the final report by Lou *et al.* (1985). The comparisons of the dimensionless maximum pressures computed numerically versus phase angle are presented in terms of time simulation in Figures 13 and 14. The numerical values and test conditions are given in Table 2. In Figure 13, a fill depth of 0.4572 m, a roll amplitude of $\theta_0 = 4^\circ$ and the amplitude of the vertical excitation $\delta_z = 0.0762$ m are taken as tank conditions. A roll amplitude of 2° with the same test conditions are taken as another comparison case in Figure 14.

The comparisons are made for the first- and second-order approximations with the experiments. The phase angle represents the angle between the rolling and vertical excitations of the tank. Zero phase angle means roll and vertical excitations are coincident. The magnitude of pressure is reduced while the phase angle δ approaches zero. The numerical model used exhibits the same tendency. In Figures 13 and 14, there is a difference between the numerical and experimental studies, especially $\delta = 0$. One possible reason is the lack of viscous effects in the numerical model in which the velocities of fluid particles are overestimated, thus the pressure. In both Figures 13 and 14, the minimum pressure values on tank walls are obtained at a zero phase angle. Note that the second-order approximation better correlates with the experimental results in Figure 14. The first-order pressure approximation, in Figure 13, gives the underestimated values except the phase angles between 50° and 85° and the second-order pressure approximation gives the overestimated values compared with the experimental results. It can be concluded from Figures 13 and 14 that the pressures under the combined roll and vertical excitations are not symmetrical in terms of phase angle.

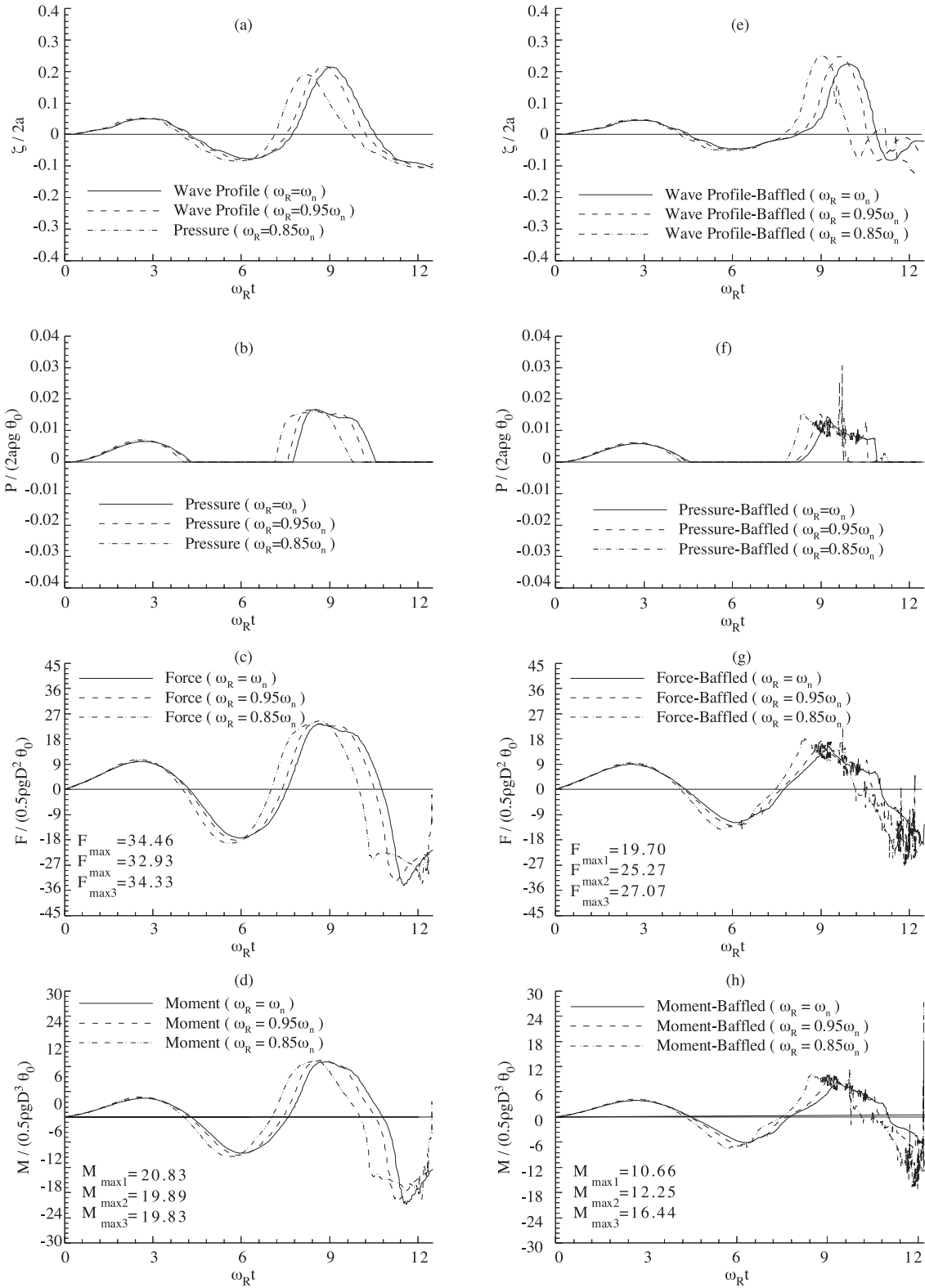


Figure 7. Comparison of the un baffled and baffled cases. Second-order approximation. ($\omega_n = 1.0596$ rad/s, $\theta_0 = 4^\circ$, $D = 0.25 \cdot H$)

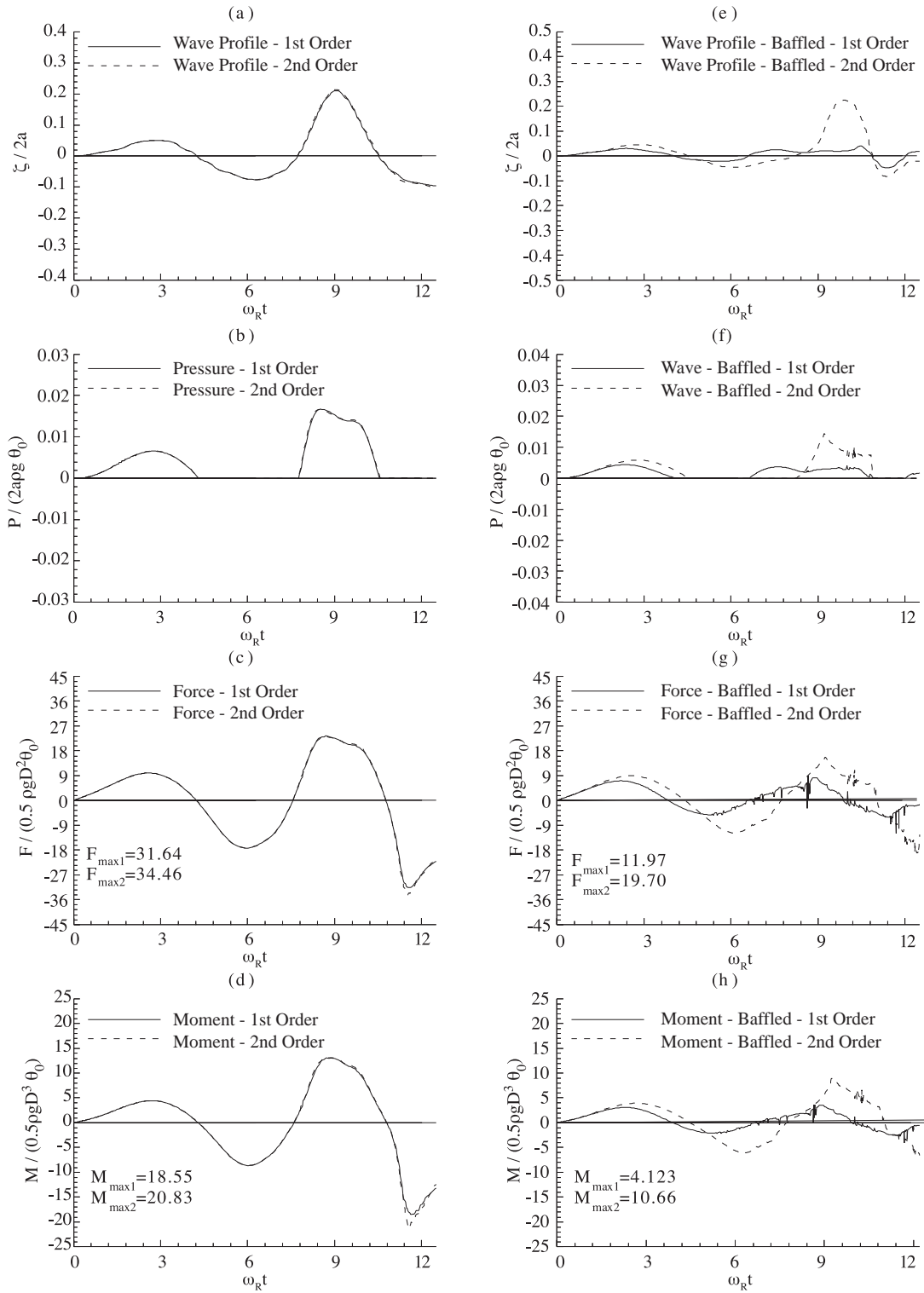


Figure 8. Comparison of the first-order and the second-order approximations. (un baffled and baffled cases, $\omega_R = \omega_n = 1.0596$ rad/s, $\theta_0 = 4^\circ$, $D = 0.25 \cdot H$)

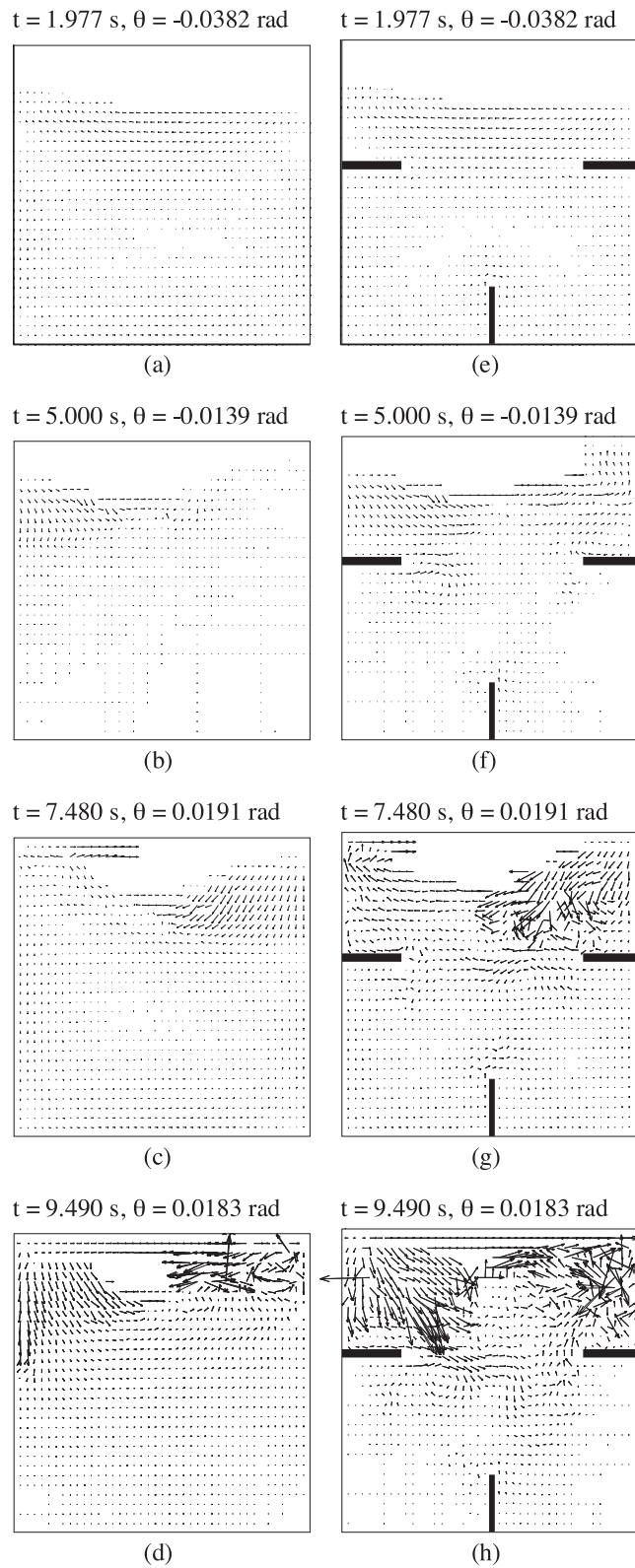


Figure 9. A snapshot for numerical simulation of the sloshing (un baffled and baffled). ($\omega_R = \omega_n = 1.2968$ rad/s, $\theta_0 = 0.0698$ rad, $D = 0.25 \cdot H$)

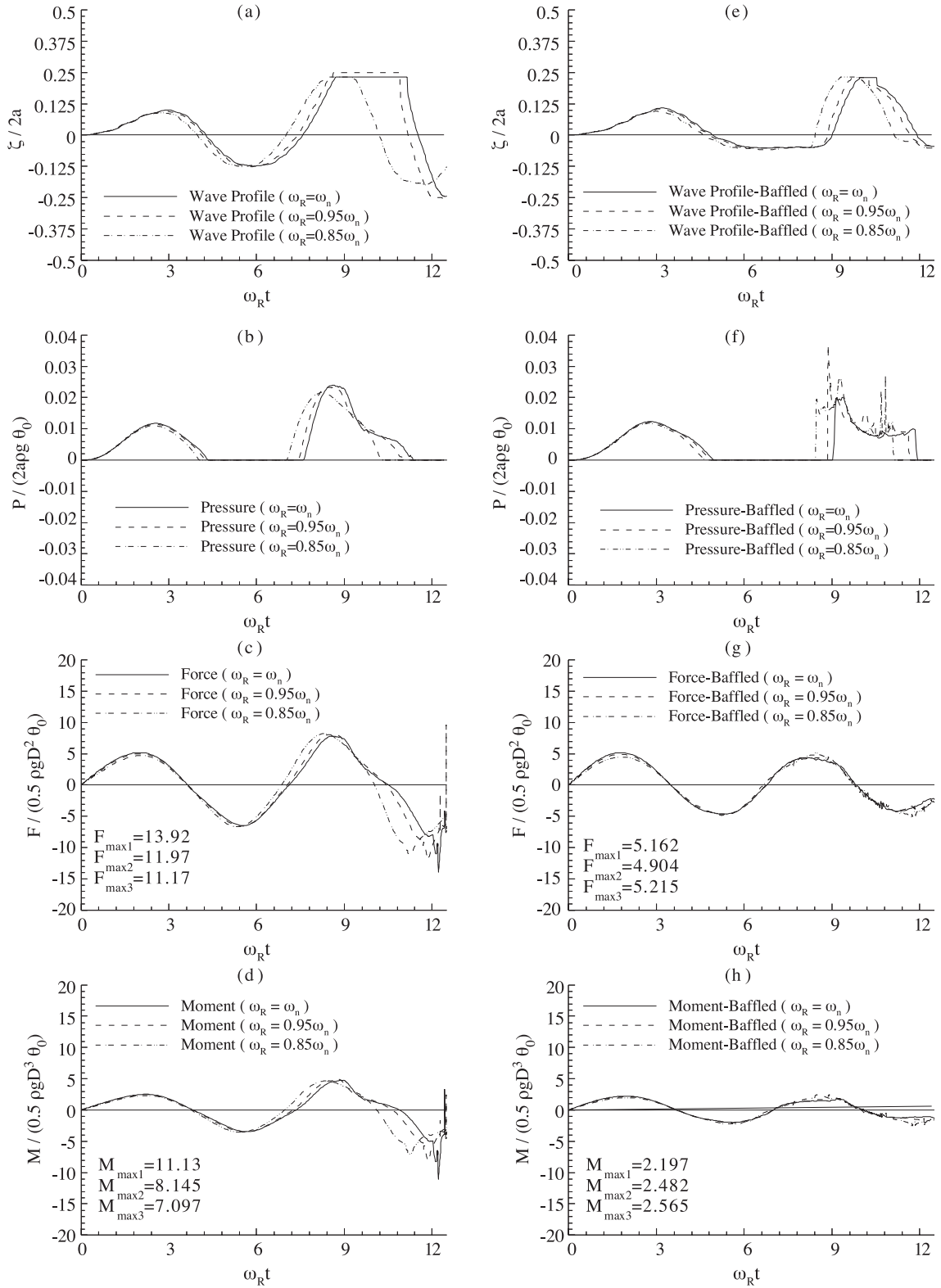


Figure 10. Comparison of the un baffled and baffled cases. First-order approximation. ($\omega_n = 1.2968$ rad/s, $\theta_0 = 4^\circ$, $D = 0.75^*H$)

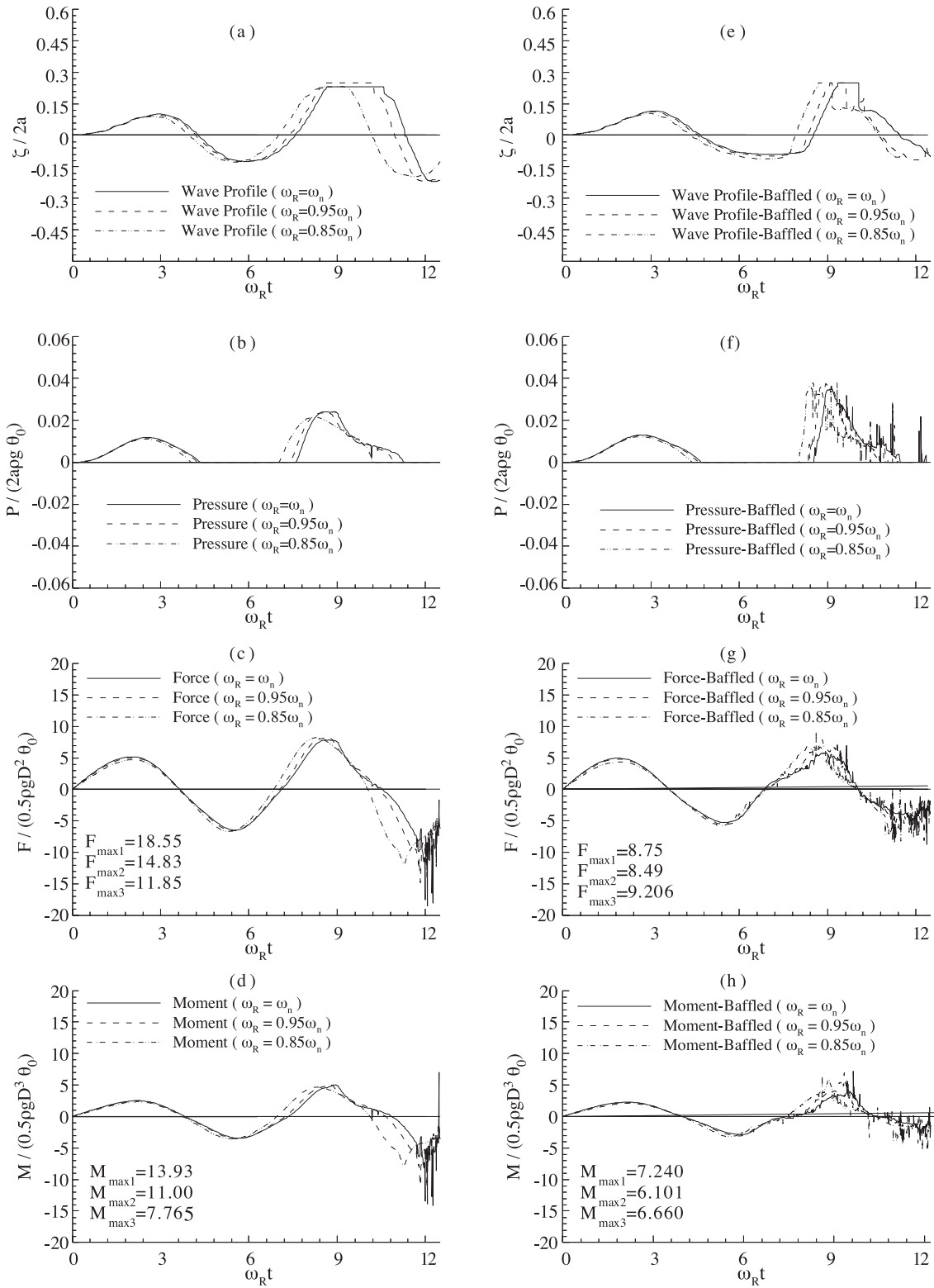


Figure 11. Comparison of the un baffled and baffled cases. Second-order approximation. ($\omega_n = 1.2968$ rad/s, $\theta_0 = 4^\circ$, $D = 0.75 \cdot H$)

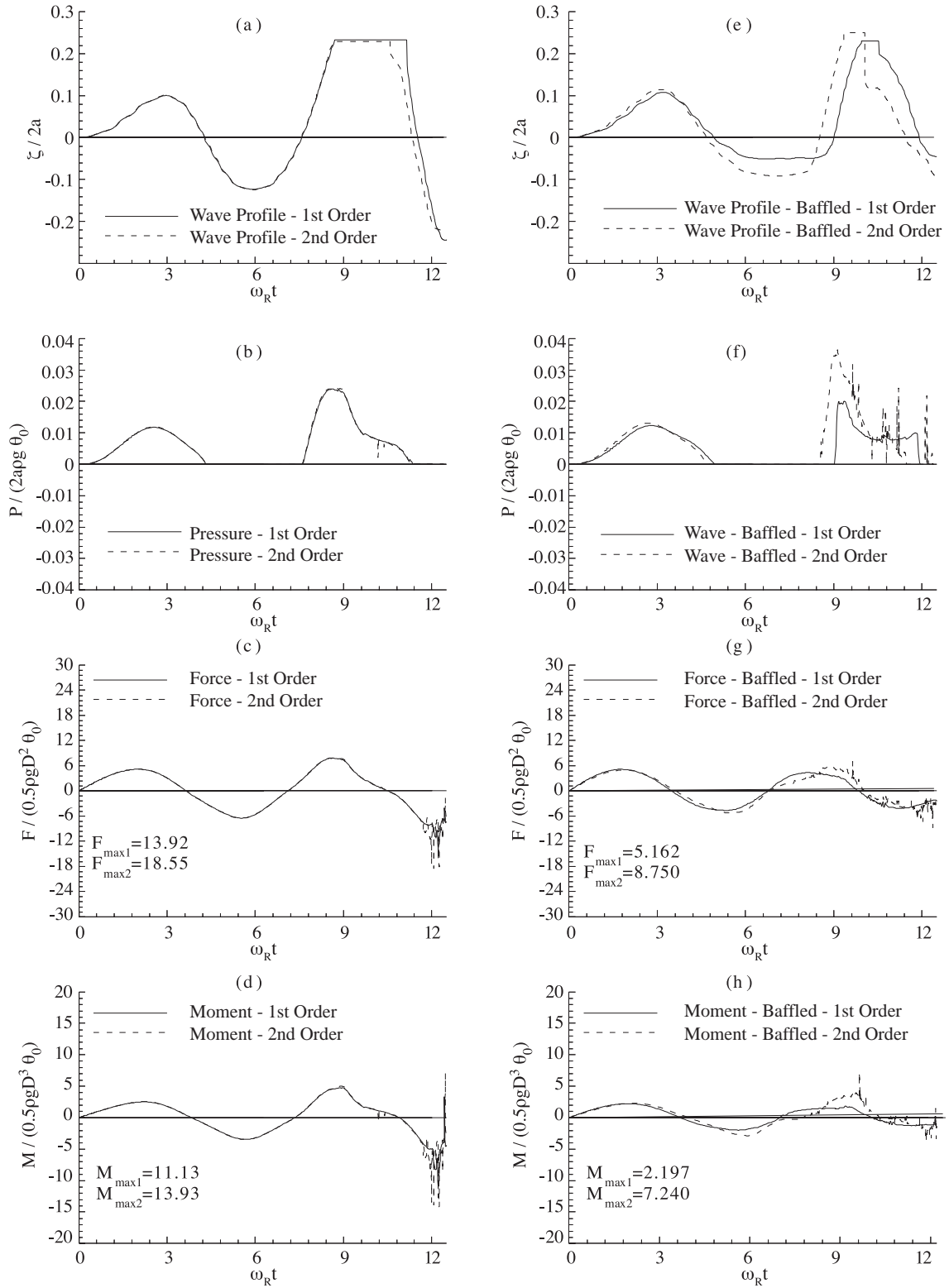


Figure 12. Comparison of first-order and second-order approximations. (un baffled and baffled cases, $\omega_R = \omega_n = 1.2968$ rad/s, $\theta_0 = 4^\circ$, $D = 0.75 \cdot H$)

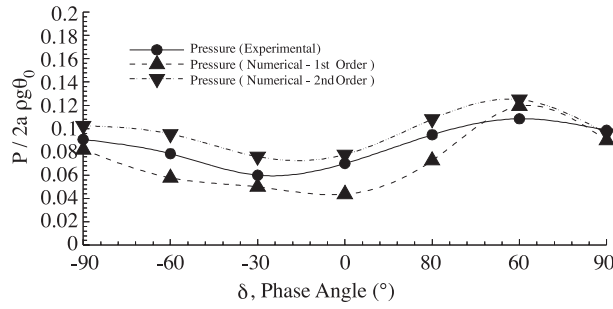


Figure 13. Comparison of the pressure values under combined roll and vertical excitations. ($2a = 0.6096$ m, $D/2a = 0.75$, $\theta_0 = 0.0698$ rad, $\delta_z = 0.0762$ m)

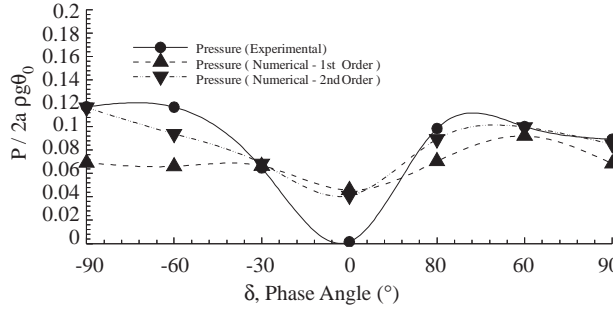


Figure 14. Comparison of the pressure values under combined roll and vertical excitations. ($2a = 0.6096$ m, $D/2a = 0.75$, $\theta_0 = 0.0349$ rad, $\delta_z = 0.0762$ m)

Table 2. Test conditions and maximum pressures values ($D = 0.4572$ m , $2a = 0.6096$ m).

$D / 2a = 0.75, \omega_n = 7.0467$ rad/s, $T / T_n = 0.959$							
$\theta_0 = 0.0698$ rad, $\delta_z = 0.0762$ m				$\theta_0 = 0.0349$ rad, $\delta_z = 0.0762$ m			
Phase Angle δ (°)	$P_{max}(exp.)$	$P_{max}(Num.)$ 1st Order	$P_{max}(Num.)$ 2st Order	Phase Angle δ (°)	$P_{max}(exp.)$	$P_{max}(Num.)$ 1st Order	$P_{max}(Num.)$ 2st Order
-90	0.0907	0.0819	0.1025	-90	0.1169	0.0691	0.1163
-60	0.0784	0.0577	0.0954	-60	0.1167	0.0660	0.0938
-30	0.0600	0.0499	0.0759	-30	0.0646	0.0664	0.0684
0	0.0700	0.0437	0.0777	0	0.0015	0.0457	0.0410
30	0.0946	0.0725	0.1081	30	0.0984	0.0703	0.0891
60	0.1084	0.1192	0.1249	60	0.1000	0.0920	0.0995
90	0.0984	0.0898	0.0960	90	0.0892	0.0683	0.0849

Conclusions

The following conclusions can be drawn from our numerical computations:

- i) The liquid responded violently causing the numerical solution to become unstable when the amplitude of excitation increased for the shallow water simulation. The instability may be related to the fluid’s motion such as the occurrence of turbulence, the transition from homogeneous flow to two-phase flow or the introduction of secondary flow along the third dimension. Thus, the applicability of the method

used in the present study is limited to the period prior to the inception of these flow perturbations.

- ii) The effect of vertical baffles was most pronounced in shallow water. For this reason, the overturning moment for both first- and second-order cases was greatly reduced.
- iii) In all cases phase shifting is observed in terms of both rolling frequency and ω_{Rt} .
- iv) Larger forces and moments were obtained by reducing fill depth due to the increasing free surface effects.

- v) In the combined roll and vertical excitation of a tank, the minimum pressures are obtained in the zero phase angle. The pressures are also not symmetrical in terms of the phase angle.

Model studies for sloshing under multi-component random excitations with phase difference should be carried out to investigate sloshing loads under more realistic tank motion inputs. Additionally, an integrated design synthesis technique must be developed to accurately predict sloshing loads for design applications.

Nomenclature

P	: fluid pressure
\mathbf{g}	: gravitational acceleration
γ	: specific weight of the fluid
θ	: roll angle
ϕ	: equilibrium angle of the tank relative to the axis of rotation
D	: fill depth

δ	: phase angle between roll and vertical excitation
δ_z	: amplitude of the vertical excitation
\mathbf{c}	: speed of sound
d	: distance between the origin of the moving coordinate and the axis of rotation
$2a$: tank length
δt	: time increment
δP	: change in pressure
ω_R	: roll frequency
ω_n	: natural frequency
$\mathbf{U}_{i,j}$: horizontal velocity of the fluid
$\mathbf{V}_{i,j}$: vertical velocity of the fluid
$\delta \mathbf{x}_i$: mesh spacing along the x-axis
$\delta \mathbf{y}_j$: mesh spacing along the y-axis
$\mathbf{F}(\mathbf{i},\mathbf{j})$: function representing the fractional volume of the fluid
H	: height of the tank

Acknowledgment

The authors would like to thank the Research Fund of İstanbul Technical University for its financial support of this study.

References

- Akyıldız H. and Çelebi M.S., “A Liquid Sloshing in a Moving Rectangular Tank”, Department Report TR 01/02, Department of Ocean Eng., Faculty of Naval Arch. and Ocean Eng., I.T.U., Turkey, 2001a.
- Akyıldız H. and Çelebi M.S., “Numerical Computation of Pressure in a Rigid Rectangular Tank Due to Large Amplitude Liquid Sloshing”, Turkish J. Eng. Env. Sci., 25, 6, 659-674, 2001b.
- Çelebi M.S. and Akyıldız H., “Nonlinear Modelling of Liquid Sloshing in a Moving Rectangular Tank”, Ocean Engineering Journal, 29, 12, 1527-1553, 2002.
- Faltinsen O.M. and Timokha A.N., “An Adaptive Multimodal Approach to Nonlinear Sloshing in a Rectangular Tank”, Journal of Fluid Mechanics, 432, 167-200, 2001.
- İbrahim R.A., Pilipchuk V.N. and Ikeda T., “Recent Advances in Liquid Sloshing Dynamics”, Applied Mechanical Review, 54, 2, 133-199, 2001.
- Lou Y.K., Su T.C. and Flipse J.E. “A Nonlinear Analysis of Liquid Sloshing in Rigid Containers”, US Department of Commerce, Final Report, MA-79-SAC-B0018, 1980.
- Lou Y.K., Wu M.C. and Lee C.K. “Further Studies on Liquid Sloshing”, US Department of Transportation, Final Report, MA-RD-760-85009, 1985.
- Lui, A.P., Lou, J.Y.K., “Dynamic Coupling of a Liquid Tank System under Transient Excitations.”, Ocean Engineering Journal, 17, 3, 263-277, 1990.
- Su T.C., Lou Y.K., Flipse J.E. and Bridges T.J. “A Numerical Analysis of Large Amplitude Liquid Sloshing in Baffled Containers”, US Department of Transportation, Final Report, MA-RD-940-82046, 1982.